

Hyperspectral Image Super-Resolution via Dual-domain Network Based on Hybrid Convolution

Tingting Liu , Yuan Liu , Chuncheng Zhang , Xiubao Sui , Qian Chen

Abstract—Since the number of incident energies is limited, it is difficult to directly acquire hyperspectral images (HSI) with high spatial resolution. Considering the high dimensionality and correlation of HSI, super-resolution (SR) of HSI remains a challenge in the absence of auxiliary high-resolution images. Furthermore, it is very important to extract the spatial features effectively and make full use of the spectral information. This paper proposes a novel HSI super-resolution algorithm, termed dual-domain network based on hybrid convolution (SRDNet). Specifically, a dual-domain network is designed to fully exploit the spatial-spectral and frequency information among the hyper-spectral data. To capture inter-spectral self-similarity, a self-attention learning mechanism (HSL) is devised in the spatial domain. Meanwhile the pyramid structure is applied to increase the acceptance field of attention, which further reinforces the feature representation ability of the network. Moreover, to further improve the perceptual quality of HSI, a frequency loss(HFL) is introduced to optimize the model in the frequency domain. The dynamic weighting mechanism drives the network to gradually refine the generated frequency and excessive smoothing caused by spatial loss. Finally, In order to better fully obtain the mapping relationship between high- resolution space and low-resolution space, a hybrid module of 2D and 3D units with progressive upsampling strategy is utilized in our method. Experiments on a widely used benchmark dataset illustrate that the proposed SRDNet method enhances the texture information of HSI and is superior to state-of-the-art methods.

Index Terms—hyperspectral image, super-resolution, dual-domain learning network, attention mechanism, frequency loss, progressive upsampling, 2D and 3D units .

I. INTRODUCTION

Hyperspectral imaging techniques is able to obtain rich spectral information of a target or a scene by the hyperspectral imaging system. Each object has different spectral characteristics. Different targets are distinguished by comparing their spectral characteristics. Therefore, hyperspectral images are employed in a variety of tasks[1], [2], [3], [4], [5], [6]. Since hyperspectral image acquisition devices usually sacrifice spatial resolution for higher spectral resolution, resulting in unsatisfactory imaging quality of hyperspectral image(HSI) [7], [8], [9]. The limited spatial resolution will lead to the mixing of end-member spectra, which affects the recognition ability of HSI.

Image super-resolution (SR) is the use of low-resolution (LR) images to recover high-resolution (HR) images, overcoming the inherent resolution limitations of imaging systems [10]. Due to the powerful representation capabilities of CNN, many novel CNN networks [11] have emerged to improve SR performance. Compared with RGB images, the spectral information of HSI needs to be considered during resolution reconstruction. More importantly, the larger the upsampling factor, the more severe the problems of texture blur and spectral distortion. For the HSI SR task, there are two main approaches, which are the fusion method with other high spatial resolution images and the single image super resolution (SISR) method. Image fusion has been shown to be useful [12], [13], [14], [15], [16]. However, there is time difference in the acquisition of auxiliary images by the imaging sensors, which the fusion approaches cannot always achieve good results. Referring to the SR method of RGB and considering the characteristics of HSI, various SISR methods based on CNN networks are designed. For instance, Li et al [17] suggested a group recurrent network (GDRRN) with global residual structure,

which inspired by recursive residual networks [18]. To avoid spectral distortion and optimize network parameters, the method relates a spectral angle mapper(SAM) to the mean square error (MSE). Jia et al [19] presented a spatial-spectral model with a single-band input. Zheng et al [20] adopted a network that the separable spectral with inception (SSIN) to improve the image resolution, and further avoid spectral distortion. The above types of algorithms have poor performance which the lack of use of spectrum information.

Since hyperspectral images have spectral dimensions, the SISR methods employing 3D convolution have certain advantages [21], [22], [23]. Mei et al. devised a CNN-based HSI SR method, termed 3D-FCNN to explore spatial-spectral correlations [21]. The network achieves better performance due to the consideration of spectral information. But regular 3D convolution kernels are adopted, which results in a large number of network parameters. Even though it has achieved some results, but is not optimal. With this shortcoming in mind, the researcher modifies the convolution kernel $k \times k \times k$ to $1 \times k \times k$ and $k \times 1 \times 1$ [23], [24], [25], [26], [27]. Such as MCNet [23] and the Spatial Spectral Residual Network (SSRNet) [24] methods. By doing this, the model parameters are greatly reduced, allowing for a more in-depth design of the network. All layers of the SSRNet are performed through the above operations. The MCNet is a hybrid convolutional approach that designs multiple 2D and 3D modules to share network parameters. This model effectively addresses the short-comings that exist in SSRNet. but its computational complexity and large number of parameters cause the network to be not optimal. Therefore, it is key to build a suitable model for HSI SR and efficiently learn the spatial-spectral depth features while addressing the above issues. The existing methods mainly extract spatial spectral information by the 2D or 3D convolution[17], [19], [20], [21]. However, such a network architecture may not be optimal, affecting performance. Although both 2D and 3D convolution are utilized[23], the number of parameters is large. Also existing methods mostly focus on low- frequency pixels in the spatial domain,

making the composite image more blurry.

To address these challenging problems, a approach of HSI SR is presented, termed dual-domain network based on hybrid convolution(SRDNet). Our main contributions are as follows.

1) Considering the high spectral dimensionality of the image, the spatial mapping relationship between low resolution and high resolution can hardly be fully acquired by one upsampling. A hybrid convolutional of 2D and 3D modules with progressive upsampling is designed, in which the 2D module is used to reinforce the spatial resolution, and the 3D module is used to extract the spectral dimension information.

2) In the 2D module, the IGM module is adopted that enables fine and diversified feature expression to address challenge details. The IGM module includes symmetric group convolution blocks and complementary convolution blocks, which enhances the internal and external relationships between individual channels by the parallel manner for facilitating different types of low-frequency structural information.

3) To better exploit the spectral prior to enhance the learning of spatially global information and spectral coherence, a dual-domain network for SR is proposed. Specifically, in the spatial domain, the self-attention module(HSL) with pyramidal structure can not only focus on the receptive field, but also model the spectral features with the global spatial spectral context, which enables feature interactions to make different contributions in reconstruction. In the frequency domain, the hyper-spectral frequency loss (HFL) is utilized to optimize the model generated by the Fourier transform, and to improve image quality by the dynamic weighting mechanism.

The other sections of this article are organized as follows: The work related to HSI SR is presented in Section II. The proposed SRDNet method is described in Section III, which includes the network structure and the dual-domain mechanism. Then, Section IV reports the experimental parameter settings and experimental analysis. Finally, Section V gives the conclusion.

II. RELATED WORK

Some of the works most relevant to our approach are briefly reviewed, including CNN-based methods, attentional mechanisms, and the use of frequency domain analysis in SISR.

A. Single HS Image Super-resolution

Early works mainly represented HSI SR as a problem of constrained optimization where some priors were used to constrain the space [28]. For example, to explore the non-local similarity in the spatial domain, the global correlation in the spectral domain, and the smooth structure of the spatial domain-spectral domain, Wang et al [29] simulated these three properties of HSI. With the help of sparse and low-rank properties, Huang et al. [30] performed reconstruction for spatial super-resolution of HSI. In recent years, due to the powerful feature extraction and representation capabilities of CNNs, traditional solutions for optimized SR are becoming obsolete. Firstly, in order to ensure the spectral properties of the intermediate results, Xie et al. [31] and Yuan et al [32] used DCNN networks with non-negative matrix decomposition for the resolution of HSIs. Due to the large number of spectral dimensions and the lack of sufficient training samples, it is difficult for DCNN networks to fully utilize the spatial and spectral properties of HSI. Mei et al [21] constructed a neural networks, termed 3D-FCNN, in which 3D convolution were applied to jointly explore spatial texture features and spectral correlations. Although it mitigates the distortion of the spectrum, it is computationally expensive at large upsampling factor. To better explore the correlation between spectral bands, Li et al [17] proposed a grouping strategy, namely the GDDRN method with recursive module. To reduce spectral distortion, the method combines a spectral angle mapper (SAM) with mean squared error (MSE). However, its lossy function affects the improvement of spatial resolution. In order for spatial and spectral information to be explored simultaneously, Hu et al. [33] combined a collaborative non-negative matrix factorization (CNMF) strategy with the results of a deep feature extraction network for learning. Although the

method work well, it considers spatial and spectral features separately and relies too much on manual. To obtain the information of each spectral band, Zheng et al [34] designed a separable spectral convolution. However, with hundreds of spectral bands it would produce a number of redundant features, making it difficult to identify the most representative fraction. Jiang et al. [25] introduced a model that extracts each group of features independently and reconstructs the HR results in an incremental manner.

Li et al. [15] suggested a network with an attention mechanism, which is known as 3D generative adversarial network to reduce the problem of inter-spectral distortion. However, the regular 3D convolution usually has storage complexity and high computational. To better learn spatial and spectral features, Li et al. designed a hybrid network by the 2D convolution and the 3D separable convolution [23]. But it has many network parameters, and the designed network structure leads to information redundancy.

Although these HSI SR methods have achieved impressive results, on the one hand, the existing methods focus on learning the spatial-spectral information of HSI from the spatial domain. The spatial domain loss function is usually applied, while the consistency of the HSI frequency domain is not well modeled. We tackle the difficult to synthesize high frequencies by subsequent modeling of SR results. Concretely, a separate module is applied to the forcing model that adaptively recovers high and hard frequencies, resulting in a higher resolution of the internal features. On the other hand, some algorithms do not selectively focus on important features and lack a global context to model spectral dependencies. Features at certain locations and in certain channels are more useful for SR reconstruction. To make fuller use of the features, a novel spatial-spectral self-attention mechanism is devised in our method, which can acquire more detailed information to suppress other useless informationn.

B. Attention Mechanism

The attention mechanism is a signal processing mechanism that obtains the focus of attention by

scanning the image, allocating more attention to the focus, attending to the details of the target, and suppressing other irrelevant information. To obtain the correlation between the spectral bands, Hu et al. designed a SENet network with a global loss function [35] and adaptively corrected the weights of the channels. Woo et al [36] and Park et al [37] calculated complementary attention along the spatial axes and the channel in turn to further improve the representation capabilities of network. The attention mechanisms can be used in SR tasks to focus on prominent information, suppress image noise and improve the performance of reconstructed images. In order to focus more on spectral characteristics, some SR methods draw on attention mechanisms from other vision tasks [38], [39], [40]. Kim et al. [41] designed a novel attention network for SR, taking into account the different differences between SR and else tasks. Dai et al. introduced second-order channels to enhance feature representation and feature learning in order to capture long-range contextual spatial information [42]. To improve the low and high frequency components of the features, Chen et al [43] raised an attention mechanism based on the feature maps for SR reconstruction in 2021. The attention mechanisms have been applied to HSI SR because of their powerful representational abilities [11]. But most existing methods discard the internal resolution of attention to accelerate computations, which results in degraded algorithm performance. The existence of some pixel-level attention mechanisms that are designed for advanced tasks [44], [45] that further enhance the representational capabilities of the model. It is essential to explore a pixel-level attention mechanism that can improve the effectiveness of HSI reconstruction.

C. Image Frequency Domain Analysis

Spectrum analysis can break down a complex signal into simpler signals. F-Principle [46] proved that the deep learning methods tend to focus on low frequency to reconstruct targets, which leads to frequency-domain differences. Recent years, the amount of CNN-based methodologies have been introduced to analyze the frequency domain. A coordinate based MLP with Fourier transform and

positional coding [47] was employed to recover high frequencies missing in single image reconstruction. Recent works have demonstrated that frequency analysis can be combined with SR [48], [49]. For example, some works have attempted to reconstruct better visual images by reducing the frequency domain difference between input and output during training [50]. The DASR [45] utilized frequency domain gaps and distances to resolve for frequency domain bias in SR. In HSI SR, where the model is more likely to focus on low-frequency pixels in the spatial domain, the composite image becomes more blurred. Therefore, exploring an adaptive constraint based on the intrinsic frequency is crucial for reconstructing fine images.

III. THE PROPOSED METHOD

A. Overall Architecture

In this subsection, the detailed overall architecture of SRDNet is presented, and its algorithm model diagram is demonstrated in Fig.1. Our method consists of four main components: the shallow feature extraction, deep spatial-spectral feature extraction, upsampling and a reconstruction part are included. For HSI super resolution, The $I^{LR} \in \mathbb{R}^{C \times H \times W}$ and the $I^{SR} \in \mathbb{R}^{C \times rH \times rW}$ are denoted the LR of input and reconstructed SR image, individually. The W and H are denoted the width and height of HSI, and C is denoted the number of channels in the HSI. The r is the size of SR scale factor that generated by the LR. Our aim is to reconstruct the SR(I^{SR}) end-to-end by network (SRDNet) from the LR (I^{LR}), as shown in Eq.(1).

$$I_{SR} = H_{Net}(I_{LR}) \quad (1)$$

where HNet(\cdot) is denoted the function of the proposed super-resolution network. The flow of the overall network architecture is as follows:

Firstly, the convolutional layer and the first residual block are defined as $F_{conv}(\cdot)$ and $F_{Res}^{(1)}(\cdot)$, respectively, through which the shallow features are extracted. The corresponding feature x_0 is defined as:

$$x_0 = F_{Res}^{(1)}(F_{conv}(I_{LR})) \quad (2)$$

Secondly, the parallel structure 2D/3D module (PAM) and the second residual block $F_{Res}^{(2)}(\cdot)$ are

adopted to extract the deep features. In order to alleviate the disappearance of HSI gradient and effectively improve the performance of method, we add a residual connection in the model. The shallow network retains more edge and texture features from HSI, while the residual connection combines shallow features x_0 with deep features x_t to further improve model information flow and the stability. The corresponding feature x_t is defined as:

$$x_t = F_{Res}^{(2)}(F_{PAM}(x_0) + F_{L_up}(x_0 \uparrow, r)) \quad (3)$$

Finally, there is the upsampling and reconstruction part, in order to upgrade the acquired features to the target size, where the upsampling module is introduced to generate a spatial spectral feature map of the target. To alleviate the affordability of the final SR reconstruction, the strategy of progressive upsampling is applied in this paper, which is divided into local upsampling and global upsampling. The $F_{L_up}(x_0 \uparrow)$ denotes the local bicubic operation. After

upsampling, the convolutional layer reconstruction operation and residual are utilized to reconstruct the HSI. The corresponding feature x_{up} is defined as:

$$x_{up} = F_{G_up}(x_t, r) \quad (4)$$

Where $F_{G_up}(\cdot)$ is denoted the global upsampling operation, where the transposed 2D convolutional layer is applied to upsample the feature map by the scale factor r .

$$x_{rec} = F_{conv}(x_{up}) \quad (5)$$

Where x_{rec} is represented convolutional layer reconstruction. The corresponding network feature output I_{SR} is expressed as follows.

$$I_{SR} = x_{rec} + F_{up}(I_{LR} \uparrow, r) \quad (6)$$

$$\text{That is } I_{SR} = F_{Rec}(F_{G_up}(x_t, r)) + F_{up}(I_{LR} \uparrow, r)$$

where $F_{up}(I_{LR} \uparrow)$ represents the input I_{LR} for up-sampling operation by bicubic interpolation. Equation (6) is equivalent to Eq. (1).

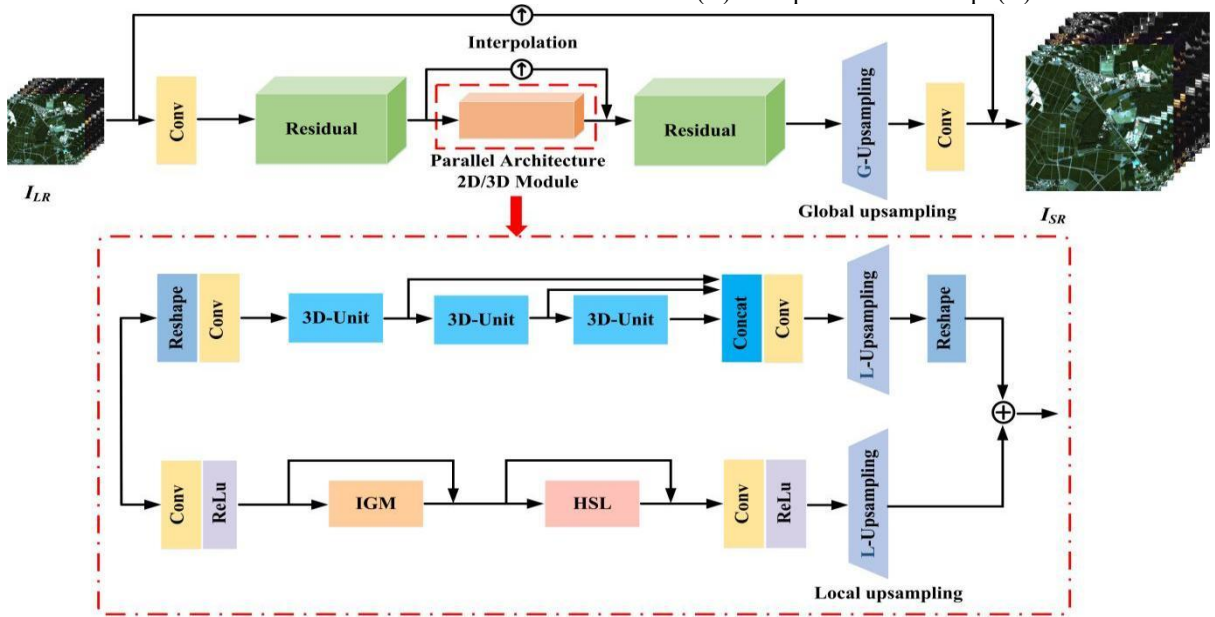


Fig.1. Overall architecture of our proposed SRDNet

The process of the overall network architecture has been described above. Next, we will introduce the network sub-modules in both the spatial-spectral domain and the frequency domain, respectively. The parallel architecture 2D/3D module will be elaborated from the spatial domain. In addition, the hyper-spectral frequency loss (HFL) will be described in detail from the frequency domain.

B. Parallel architecture 2D/3D module(PAM)

After shallow feature extraction, the information flow is divided into two branches, which the first is a 3D convolutional branching sub-network and the second is a 2D convolutional branching sub-network.

1) 3D Unit Branch Network

As mentioned in the second subsection, HSIs have extra spectral dimension compared to RGB images, which allows the use of 3D convolution to gain information beyond the spatial dimension. Therefore,

3D convolutions can be introduced to acquire spatial and spectral characteristics from HSIs. Separable convolution has been explained to have comparable performance to standard 3D convolution [51], with a much lower number of model parameters. To decrease the number of parameters, this paper makes use of separable 3D convolution (the convolution kernel of filter $k \times k \times k$ is replaced with $k \times 1 \times 1$ and $1 \times k \times k$) instead of the standard 3D convolution. To be able to use 3D convolution, since size of the input HSI is $C \times W \times H$, the I_{LR} is reshaped into four dimensions ($1 \times C \times W \times H$).

$$y_0^{3D} = f_{1 \times 1 \times 1}^{3D}(f_{Reshape}(x_0)) \quad (7)$$

where $f_{Reshape}(\cdot)$ is denoted the extended dimension of the feature map that extracts from the first residual group block, and $f_{1 \times 1 \times 1}^{3D}(\cdot)$ denotes the 3D convolution $1 \times 1 \times 1$ operation. As for 3D-Unit, as shown in Fig. 2. The $1 \times k \times k$ convolution kernel is used to extract spatial features, while the $k \times 1 \times 1$ convolution kernel is used to learn spectral information.

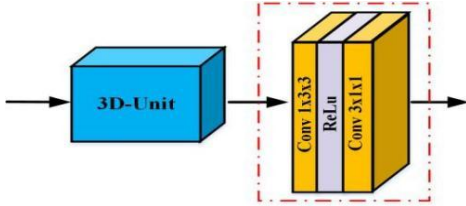


Fig.2. Architecture of 3D-unit

The kernel is the same for each 3D-Unit, and in the case of the first 3D-Unit, the output can be represented as follows.

$$y_{1D}^{3D} = \sigma(f_{3 \times 1 \times 1}^{3D}(\sigma(f_{1 \times 3 \times 3}^{3D}(y_0^{3D})))) \quad (8)$$

Output of the previous 3D-Unit is employed as input to the next 3D-Unit. Assuming that there are N 3D-Units in the model, the output is shown as:

$$y_{ND}^{3D} = f_{ND}^{3D}(f_{(N-1)D}^{3D}(\dots f_{2D}^{3D}(f_{1D}^{3D}(y_0^{3D})))) \quad (9)$$

Where $f_{ND}^{3D}(\cdot)$ is represented the Nth 3D-Unit operation (in order to make the network simple and effective, here $N=3$). After obtaining hierarchical features through N 3D-Units, their outputs are cascaded together to allow the network to obtain more useful information. After the $1 \times 1 \times 1$ convolution fusion $f_{1 \times 1 \times 1}^{3D}(\cdot)$, local upsampling is performed, and the corresponding feature operations are as follows.

$$y_{Concat}^{3D} = \sigma(f_{1 \times 1 \times 1}^{3D}(f_{Concat}^{3D}[y_{1D}^{3D}, y_{2D}^{3D}, y_{1D}^{3D}]))$$

$$y_{L_up}^{3D} = f_{L_up}^{3D}(y_{Concat}^{3D}) \quad (10)$$

Among them, the y_{Concat}^{3D} is represented the operation of each 3D-Unit output cascade $f_{Concat}^{3D}(\cdot)$, and the $f_{L_up}^{3D}(\cdot)$ is represented a local upsampling operation. Finally, the obtained feature $y_{L_up}^{3D}$ is reshaped from four dimensions ($1 \times C \times W \times H$) to the image size of three dimensions ($C \times W \times H$). The output of the 3D Unit branch is obtained, i.e.

$$y^{3D} = f_{Reshape}(y_{L_up}^{3D}) \quad (11)$$

where is denoted the feature dimension that is denoted the feature dimension that is squeezed .

2) 2D Unit Branch Network:

Unlike the 3D-Unit operation, the 2D Unit branching network is used to further extract deep features through the IGM unit. The structure of which is displayed in Fig. 3.

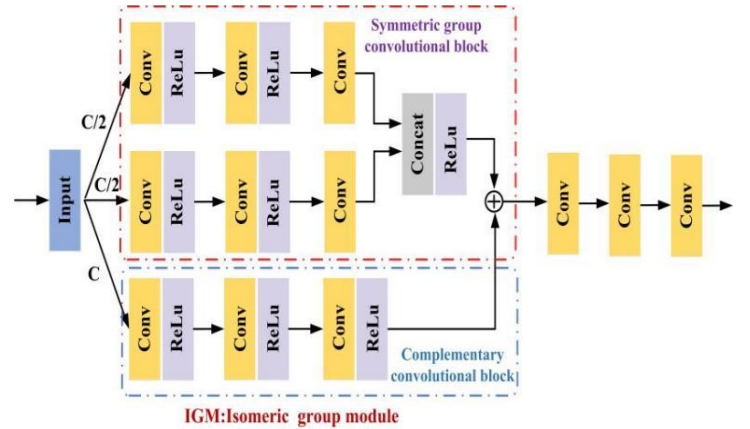


Fig.3. IGM structure diagram

a) Isomeric Group Module(IGM) module

Inspired by the [52], we design the IGM module. Previous HSI SR work directly fuses the layered features of entire channels to improve the image resolution performance, which likely increase the redundant features and the convergence time of the algorithm. To address this challenge, we adopt the IGM module by interacting various channels to gain deeper low-frequency information, thereby enhancing the relationship between different channels and improving SR algorithm performance. Specifically, the IGM consists of symmetric group convolution blocks and complementary convolution blocks. The internal and external relationships of the various

channels are enhanced by the parallel manner to acquire different types of more representative structural information.

Symmetric group convolution block: There are two 3-layer branch sub-networks in the symmetric group convolution block, which obtain the main information of the channel, respectively. The acquired features are integrated to enhance their internal correlation in the image by cascading operations. In particular, each layer of tributary sub-network is Conv+ReLU. Also, each layer has 32 input and output channels respectively, and their convolution kernels are 3×3 . The output of the symmetrical group block is operated in output cascade via two branched sub-networks, resulting in 64 output channels. Two of the branch sub-networks have the same structure. Here, as an instance, output of the first branch sub-network is represented as:

$$\begin{aligned} x_0^{2D} &= \sigma(f_{conv}^{3 \times 3}(x_0)) \quad (12) \\ y_{1b}^{2D} &= \sigma(f_{conv}^{3 \times 3}(x_0)) \\ y_{SGB-1}^{2D} &= f_{3b}^{2D}(f_{2b}^{2D}(y_{1b}^{2D})) \end{aligned}$$

Where $f_b^{2D}(\cdot)$ is denoted the operation of 3×3 convolution and ReLU function per layer, for a total of 3 layers.

Similarly, the second branch sub-network is the same as the first operation, and the output feature representation:

$$y_{SGB-2}^{2D} = f_{3b}^{2D}(f_{2b}^{2D}(y_{1b}^{2D})) \quad (13)$$

After cascading the output features of the two branched sub-networks, the output features of the symmetric group of convolutional blocks are obtained, i.e. the output feature representation of this network.

$$y_{SGB}^{2D} = f_{Concat}^{2D}[y_{SGB-1}^{2D}, y_{SGB-2}^{2D}] \quad (14)$$

Complementary convolution block: The complementary convolutional block has only one 3-layer branched sub-network, taking into account the overall of all channels. The complementary convolutional block are utilized to enhance their external correlation and robustness of the algorithm, which is replenishment to the symmetric group convolution block. Each layer of the complementary convolution

block is the same as the symmetric group convolution block, that is, each layer consists of Conv+ReLU. But the difference is that the convolution input with output channels for each layer are 64, and the filters set to 3×3 . The output of the complementary convolution block is represented as:

$$\begin{aligned} y_{1b}^{2D} &= \sigma(f_{conv}^{3 \times 3}(x_0)) \quad (15) \\ y_{CB}^{2D} &= f_{3b}^{2D}(f_{2b}^{2D}(y_{1b}^{2D})) \end{aligned}$$

The output of symmetric group convolution blocks and complementary convolutional blocks is spatially superimposed, and adopted as the output of IGM module after convolution fusion. The residual connection allows the network to refine more efficient information. The output feature of this module is expressed as:

$$\begin{aligned} y_{IGM}^{2D} &= y_{CB}^{2D} + y_{SGB}^{2D} \quad (16) \\ y_{IGM}^{2D} &= f_{conv}(y_{IGM}^{2D}) \\ y_{IGM}^{2D} &= y_{IGM}^{2D} + x_0^{2D} \end{aligned}$$

b) HSL module

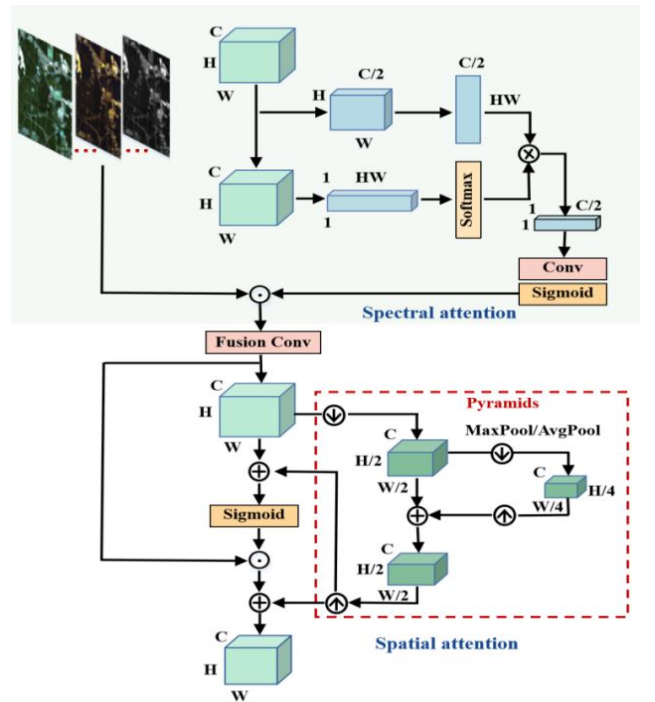


Fig.4. Hyperspectral attention mechanism

First of all, since indiscriminate treatment of all types of features in the convolution kernel, this will make the network limited in its ability to rebuild. It is difficult to distinguish useful high-frequency information from rich low-frequency features [36]. Secondly, the perceptual field of each layer of the

convolution kernel only locally expresses that the output is only partially related to the input, and it lacks sufficient contextual information. Once again, spectral features is of great significance to the HSI, so adequate exploration of spectral correlations cannot be neglected. Based on the above 3 considerations, we incorporate attention mechanisms from the spatial and spectral dimensions, respectively. This enables exploring the long-range dependence of pixel positions and the correlation of spectral bands. The specific structure is illustrated in the Fig. 4.

Spectral Attention: The convolutional layer is utilized to linearly map the input feature to obtain the *query* vector $y_{\text{Channel-q}}^{2D}$ and *key* vector $y_{\text{Channel-k}}^{2D}$. And the full space *query* vector and half channel *key* vector are obtained by Reshape operation. Then, the *query* vector is remapped to the *key* vector through the matrix multiplication operation. And the auto-correlation of the spectral dimension is calculated to obtain the attention coefficient, which is recorded as the *value* vector $y_{\text{Channel-v}}^{2D}$. Its channel is maintained as $C/2$, which prevents excessive computational cost.

$$\begin{aligned} y_{\text{Channel-q}}^{2D} &= f_{\text{Softmax}}(f_{\text{Reshape}}(f_{\text{conv}}(y_{\text{IGM}}^{2D}))) \in \mathbf{R}^{1,HW} \\ y_{\text{Channel-k}}^{2D} &= f_{\text{Reshape}}(f_{\text{conv}}(y_{\text{IGM}}^{2D})) \in \mathbf{R}^{C/2,HW} \\ y_{\text{Channel-v}}^{2D} &= y_{\text{Channel-q}}^{2D} \otimes y_{\text{Channel-k}}^{2D} \in \mathbf{R}^{C/2,1,1} \end{aligned} \quad (17)$$

where the original signal $y_{\text{IGM}}^{2D} \in \mathbf{R}^{1,H,W}$ represents the output features of the IGM module that is obtained in Eq.(17), and the $f_{\text{Reshape}}(\cdot)$ represents the vector reshape operation. The \otimes denotes the matrix multiplication operation and the $f_{\text{Softmax}}(\cdot)$ represents the Softmax function. As shown in the Fig. 4, after the *value* vector is activated by convolution and Sigmoid, weight coefficient of each channel can be acquired.

$$y_{\text{Channel-map}}^{2D} = f_{\text{Sigmoid}}(f_{\text{conv}}(y_{\text{Channel-v}}^{2D})) \in \mathbf{R}^{C,1,1} \quad (18)$$

where $f_{\text{Sigmoid}}(\cdot)$ denotes the Sigmoid activation function and $f_{\text{Channel-map}}^{2D}(\cdot)$ denotes the channel attention weight coefficient.

Finally, the original signal y_{IGM}^{2D} is multiplied by the weight factor of each channel to obtain the calibrated input signal, so that the HSI focuses on the channel with greater weight.

$$y_{\text{Channel}}^{2D} = y_{\text{IGM}}^{2D} \odot y_{\text{Channel-map}}^{2D} \in \mathbf{R}^{C,H,W} \quad (19)$$

Spatial Attention: After obtaining the attention in the spectral dimension, the spatial attention mask is

calculated for the fused features. A pyramidal design is used to increase the attentional receptive field. This is followed by element-by-element multiplication and addition, and fusion of features by mask modulation. The specific definitions are as follows:

$$y_{\text{Fusion}}^{2D} = f_{\text{conv}}(y_{\text{Channel}}^{2D}) \in \mathbf{R}^{C,H,W} \quad (20)$$

$$y_{\text{Down}}^{2D} = f_{\text{conv}}[y_{\text{max}}^{2D}, y_{\text{avg}}^{2D}] \in \mathbf{R}^{C,H/2,W/2}$$

$$y_{\text{Pyramid}}^{2D} = f_{\text{Up}}(f_{\text{Down}}(y_{\text{Fusion}}^{2D})) + y_{\text{Down}} \in \mathbf{R}^{C,H/2,W/2}$$

Where the y_{Fusion}^{2D} is denoted the fusion of spectrally corrected features, the $y_{\text{max}}(\cdot)$ and $y_{\text{avg}}(\cdot)$ are denoted the maximum pooling and average pooling operations, i.e. downsampling, respectively. The $f_{\text{Down}}(\cdot)$ is denoted the acquired post-sampling features and the $f_{\text{Up}}(\cdot)$ is denoted the upsampling operation.

As shown in the Fig. 4, the obtained features have undergone two down-sampling and upsampling respectively. Then after Sigmoid function, the weight coefficient of the spatial pixel can be obtained.

$$y_{\text{Spatial-map}}^{2D} = f_{\text{Sigmoid}}(f_{\text{Up}}(y_{\text{Pyramid}}^{2D}) + y_{\text{Fusion}}) \in \mathbf{R}^{C,H,W} \quad (21)$$

Where the $f_{\text{Spatial-map}}^{2D}(\cdot)$ is denoted the obtained spatial pixel weighting factor.

The calibrated input signal is obtained by dot producting the fused signal y_{Fusion} of spectral attention with the spatial pixel weight factor, so that the HSI focuses on the pixel area with greater weight.

$$y_{\text{Spatial}}^{2D} = y_{\text{Fusion}} \odot y_{\text{Spatial-map}}^{2D} \in \mathbf{R}^{C,H,W} \quad (22)$$

Finally, the output signals obtained from the spectral and spatial domain corrections are superimposed. And the network extracts more effective information by the residual connection. The output feature map is made to be highly correlated in both spatial pixels and spectral dimensions. This is shown in the following operation.

$$y_{\text{HSL}}^{2D} = y_{\text{Channel}}^{2D} + y_{\text{Spatial}}^{2D} \quad (23)$$

$$y_{\text{HSL}}^{2D} = y_{\text{HSL}}^{2D} + y_{\text{IGM}}^{2D}$$

where the y_{HSL}^{2D} is denoted the output characteristics of the HSL module.

Similar to the 3D branch network, in order to alleviate the burden of final SR reconstruction, the local upsampling is used. This is shown in the following operations:

$$y^{2D} = f_{L_up}^{2D}(\sigma(f_{conv}(y_{HSL}^{2D}))) \quad (24)$$

In the PAM network, outputs of the 3D Unit branch network and the 2D Unit branch network are fused from spatial pixels. The definition is shown below.

$$x_t = y^{2D} + y^{3D} \quad (25)$$

where the x_t is denoted the output of the entire PAM block, which is the result of the operation of the $F_{PAM}(\cdot)$ function in Eq. (3).

c) Hyperspectral frequency loss (HFL)

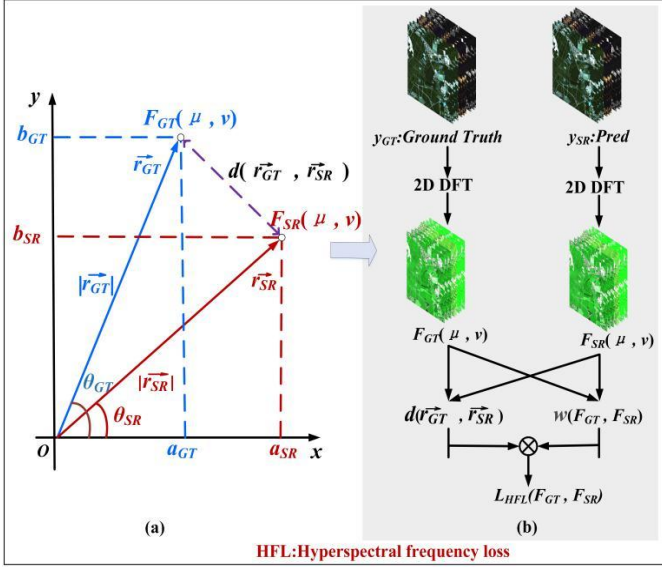


Fig.5 Hyperspectral frequency loss

The bias inherent in CNNs tends to avoid frequencies that are difficult to synthesize in the network, i.e., hard frequencies. Since each pixel has the same importance for a certain frequency, it is usually difficult to discover hard frequencies and compose them by pixel loss in spatial domain. Therefore, we introduce the frequency loss (HFL), which uses dynamic spectral weighting matrix pairs to distinguish between different frequencies. It allows the model to quickly focus on the hard frequencies, thus progressively refines the generated image frequencies to improve quality of the reconstructed image. The detailed network design is shown in Fig. 5.

Discrete Fourier Transform (DFT) image analysis: The Discrete Fourier Transform (DFT) converts discrete finite signals into their constituent frequencies. Therefore, we convert the HSI to frequency representation by 2D discrete Fourier transform, as shown in Fig. 5(b).

$$F_{(u,v)} = \sum_{x=0}^{H-1} \sum_{y=0}^{W-1} f(x,y) \cdot e^{-i2\pi(\frac{ux}{H} + \frac{vy}{W})} \quad (26)$$

where the image dimensions are $H \times W$; the (x, y) is denoted the coordinate of the image pixels in spatial domain; and the $f(x, y)$ is represented as a pixel value. The (u, v) is denoted the spatial coordinate of the spectrum; the $F(u, v)$ is the complex frequency value, which is the sum of each image pixel in the spatial domain.

HSI frequency distance analysis: As shown in Fig. 5(a), the distance metric can be used to quantify the variance between the reconstructed SR and the ground truth in the frequency domain. In the frequency domain, frequencies in the same space are used as operating objects, which are represented as different 2D sinusoidal components in the image. Amplitude and phase should be considered when utilising frequency distances as they capture different features about the image. Each frequency value is mapped into a two-dimensional space (i.e., a plane) and turned into a Euclidean vector. The distance of the frequency is converted to the distance between the \vec{r}_{GT} and the \vec{r}_{SR} , which requires consideration of both the the angle and magnitude vector (the purple line in Fig. 5(a)). We use the square of the Euclidean distance for a single frequency (the k_{th} example).

$$d_{(\vec{r}_{GT}, \vec{r}_{SR})}^k = \left\| \vec{r}_{GT}^k - \vec{r}_{SR}^k \right\|_2^2 = \left| F_{GT}^k(u, v) - F_{SR}^k(u, v) \right|^2 \quad (27)$$

Where $k = \{ 0, 1, 2, \dots, C-1 \}$, and the frequency distance between the ground truth and the reconstructed image can be written as the mean value.

$$d_{(u,v)}^k = \frac{1}{HW} \sum_{u=0}^{H-1} \sum_{v=0}^{W-1} \left| F_{GT}^k(u, v) - F_{SR}^k(u, v) \right|^2 \quad (28)$$

Due to the inherent bias, the network will still be biased towards easy frequencies, in order to achieve the training focus on hard frequencies, a spectral weight matrix $w(u, v)$ is introduced to weight the easy frequencies. The specific definition is as follows:

$$w_{(u,v)}^k = \left| F_{GT}^k(u, v) - F_{SR}^k(u, v) \right|^\alpha \quad (29)$$

where α is the scale factor for flexibility (in the experiment $\alpha=1$). Further normalize $w(u, v)$ into the $[0, 1]$ range, where the 1 corresponds to the frequency

that is currently lost the most and easy frequency. Each frequency is weighted differently.

Taking the $w(u, v)$ matrix value and the frequency distance matrix by Hadamard (shown in Fig. 5(b)), we get the output of HSI frequency loss (HFL) as follows.

$$d(F_{GT}^k, F_{SR}^k) = \frac{1}{HW} \sum_{u=0}^{H-1} \sum_{v=0}^{W-1} w_{(u,v)}^k |F_{GT}^k(u, v) - F_{SR}^k(u, v)|^2$$

$$L_{HFL}(F_{GT}, F_{SR}) = \sum_{k=0}^{C-1} d(F_{GT}^k, F_{SR}^k) \quad (30)$$

d) Total training losses

The L_1 loss is used in many SR works, which can be employed to measure the difference between predicted values and ground truth, and maintain good convergence in training. In this article, L_1 loss is applied to calculate the loss of spatial domain pixels. Meanwhile, The L_{HFL} (shown in Eq. 30) is adopted to calculate the loss in the spectral frequency domain.

$$L_1(\Theta) = \frac{1}{N} \sum_{n=1}^N \|I_{GT}^n - H_{Net}(I_{LR}^n)\|_1 \quad (31)$$

Where the I_{GT}^n and the $H_{Net}(I_{LR}^n)$ are denoted the n th ground truth and the reconstructed hyperspectral image, the N is indicated the number of HSI in a training batch, the Θ is used the parameter set of our network. The total loss L_{total} combined with dual-domain network is expressed as:

$$L_{total} = L_1 + \beta L_{HFL} \quad (32)$$

Where the β is utilized to balance the contribution of various losses. Through experiments, we found that the effect is best when $\beta=0.1$.

IV. EXPERIMENTS

A. Experiment Settings

1) Datasets

a) CAVE dataset: The CAVE database¹ was collected by a cooled CCD camera [53] in wave-lengths ranging of 400 nm-700 nm (31 bands) in steps of 10 nm. The database contains 32 object scenes where the HSIs size are $512 \times 512 \times 31$, and it is saved as a PNG image in 16-bit grayscale.

b) Harvard dataset: The Harvard dataset² was acquired through Nuance FX, CRI Inc. Cameras [54] and located in a scene of daylight or outdoors. The

dataset contains 77 HSIs, each with a size of $1040 \times 1392 \times 31$. Unlike the CAVE dataset, it is stored in the .mat format.

c) Chikusei Dataset: The Chikusei dataset³ was captured by the Headwall Hyperspec-VNIR-C sensor in Chikusei, Japan. The dataset ranges from 343 nm-1018 nm and contains 128 spectral bands, which the spatial resolution of HSIs is 2.5 meters and the size is 2517×2335 . The dataset contains both urban and rural areas with a total of 19 types of terrestrial objects.

2) Implementation Details

Each dataset is acquired by a different camera, so so they all need to be trained and tested separately. In our experiments, a random sample of 80% from the CAVE and Harvard datasets is selected for training, 10% for validation, and 10% for testing. During training, the quantities of images in these datasets is too small for the CNN algorithm. In order to avoid over-fitting, the dataset is augmented, i.e. these 24 patches are randomly selected to augment the training data. The specific operation is as follows: the patch is flipped horizontally (90° , 180° , 270°) and scaled (1, 0.5, 0.75). These patches are down-sampled to the low spatial resolution images of size $32 \times 32 \times C$ by interpolation according to a scale factor r . As described in subsection 3, the filters in each convolution layer is set to $1 \times 3 \times 3$ and $3 \times 1 \times 1$ in the 3D unit. The size of the filter in the 2D convolution is 3×3 . The amount of filters for all layers in the network is 64. During training, the optimizer selects ADAM and sets β_1 and β_2 to 0.9 and 0.999, respectively. The initial learning rate is 1.1×10^{-4} , and every 35 epochs decreases to half of the original, running a total of 200 epochs. The operating systems is the Ubuntu 18.04, and the deep learning frameworks is Pytorch 1.7.1. The Hardware Acceleration Platforms is RTX 3090 GPU, and training per batch is 32. To improve the efficiency of the test, an area of size 512×512 in the top left corner is selected as the test image for evaluation.

3) Evaluation Metrics

In our experiments, we introduced six widely quantitative image quality indices (PQI) to evaluate

¹ <https://www.cs.columbia.edu/CAVE/databases/>

² <http://vision.seas.harvard.edu/hyperspec/>

³ <https://naotoyokoya.Com/Download.html>

the effectiveness of network, among them peak signal-to-noise ratio (PSNR) and structural similarity (SSIM) [55], root mean square error (RMSE), mutual correlation (CC) [56], spectral angle mapper (SAM) [57], and error relative global adaptive synthesis (ERGAS) [58]. As for PSNR and SSIM, we evaluated the mean values of the reconstructed images in all spectral bands. And for PSNR, SSIM, RMSE are widely employed image recovery quality metrics, the optimal values for these three metrics are $+\infty$, 1 and 0 respectively. While the remaining three metrics (CC, SAM, ERGAS) are commonly applied in HSI fusion works, their optimal values are 1, 0 and 0, respectively.

B. Comparisons With Other Methods

In our experiments, we compare six existing classical approaches with the SRDNet in a comprehensive manner. These methods are Bicubic, GDRRN [17], 3D-FCNN [21], EDSR [59], SSPSR [25] and MCNet [23]. Three datasets, the CAVE, Harvard and

Chikusei, are adopted to validate the advantages of the SRDNet with different sampling factors and different number of bands.

1) Results on CAVE Dataset

TABLE I
COMPARISON OF ALGORITHMS IN TERMS OF NUMBER OF CAVE PARAMETERS

Methods	$\times 2$	$\times 3$	$\times 4$
Bicubic	-	-	-
GDRRN[17]	0.22M	0.22M	0.22M
3D-FCNN[21]	0.039M	0.039M	0.039M
EDSR[59]	1.40M	1.59M	1.55M
SSPSR[25]	10.54M	13.49M	12.90M
MCNet[23]	1.93M	2.04M	2.17M
SRDNet	1.57M	1.72M	1.60M

In Table 1, it can be seen that the number of parameters of our method is slightly more than the number of parameters of EDSR, but under the same scale factor, the proposed SRDNet can obtain the best results.

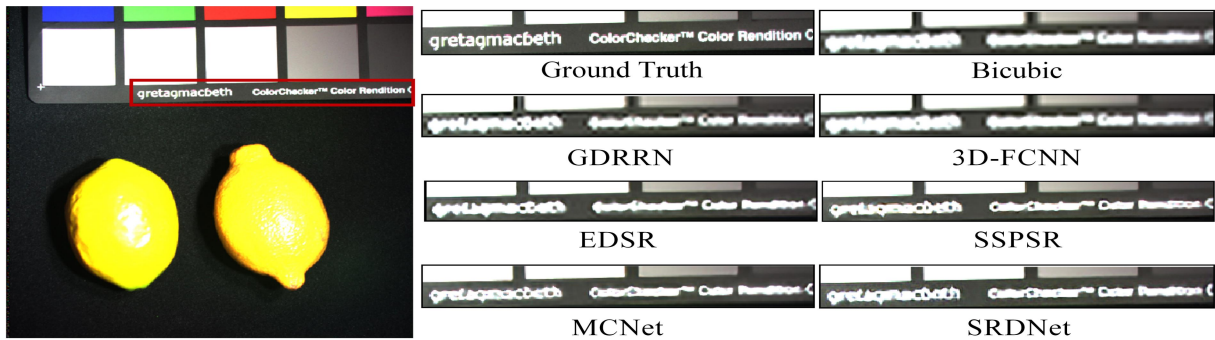


Fig.6. Reconstructed the *fake_and_real_lemons_ms* image of in CAVE dataset with spectral bands 23-15-8 as R-G-B when the upsampling factor is 4.

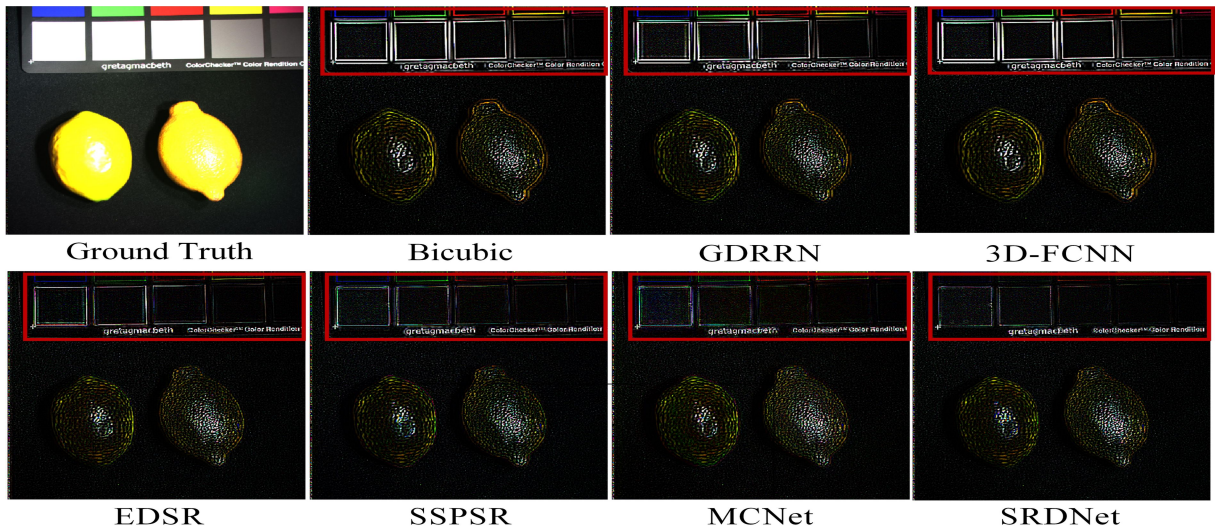


Fig.7. Absolute error map comparisons for the *fake_and_real_lemons_ms* with spectral bands 23-15-8 as R-G-B when the upsampling factor is 4. The less information the image contains, the closer the reconstructed image is to the target image.

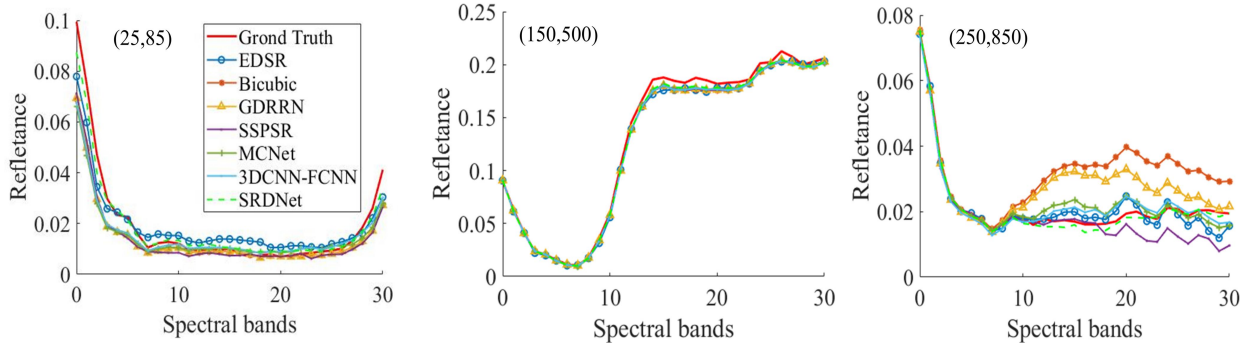


Fig.8. The visual comparison of the *fake_and_real_lemons_ms* image image spectral distortion at pixel locations (25,85), (150,500) and (250,850) on the CAVE dataset.

Fig.6 explains the reconstructed visual results for each algorithm. Fig.7 and 8 also show the difference in reconstruction information between the algorithms through error plots and spectral fitting plots. It can be observed from Table 2 and Fig.7 that all algorithms reconstruct high-resolution HSIs well, but the proposed SRDNet method performs better than the space-based prior EDSR and spectroscopic prior 3D-FCNN [21]. The SSPSR [25] and GDRRN [17] algorithms are specifically designed for HSIs, and they can sometimes obtain good results, but their

network performance seems to be unstable when working on different datasets. In table 2, the PSNR and the SSIM of SRDNet are 1.044dB/0.0014, 0.159dB/0.0006 and 0.141dB/0.0006, and it is higher than the second method(MCNet) when the up-sampling factor is 2/3/4, respectively. Specifically, the PSNR is increased by 2.3% with an upsampling factor of 2.

In addition, as shown in Table 1, the number of network parameters is less the SRDNet than the MCNet..

TABLE II

QUANTITATIVE COMPARISON OF DIFFERENT METHODS FOR THE 6 PQIS PAIRS OF 5 TEST IMAGES ON THE CAVE DATASET. RED AND BLUE SHOW THE BEST AND SECOND BEST PERFORMANCE RESPECTIVELY.

Scale	Metrics	Bicubic	GDRRN[17]	3D-FCNN[21]	EDSR[59]	SSPSR[25]	MCNet[23]	SRDNet(Our)
×2	CC↑	0.990	0.991	0.991	0.991	0.989	0.992	0.993
	SAM↓	2.605	2.609	2.605	2.905	2.823	2.417	2.264
	RMSE↓	0.008	0.007	0.007	0.006	0.006	0.005	0.005
	ERGAS↓	7.546	7.467	7.465	7.742	7.750	6.460	6.165
	PSNR↑	42.662	43.423	43.377	44.362	44.162	45.080	46.124
	SSIM↑	0.9885	0.9898	0.9864	0.9903	0.9900	0.9915	0.9929
×3	CC↑	0.983	0.984	0.985	0.988	0.988	0.988	0.989
	SAM↓	3.255	2.895	2.907	3.163	2.841	2.750	2.672
	RMSE↓	0.011	0.011	0.010	0.009	0.009	0.008	0.007
	ERGAS↓	10.290	10.871	7.937	7.909	7.908	7.795	7.766
	PSNR↑	38.988	39.337	41.345	42.432	42.132	42.785	42.944
	SSIM↑	0.9763	0.9788	0.9792	0.9859	0.9852	0.9863	0.9869
×4	CC↑	0.979	0.980	0.981	0.985	0.985	0.986	0.986
	SAM↓	3.654	3.622	3.421	3.258	3.060	3.033	3.025
	RMSE↓	0.014	0.014	0.013	0.010	0.0010	0.010	0.010
	ERGAS↓	11.278	10.311	9.911	9.171	9.147	8.905	8.272
	PSNR↑	36.853	37.164	38.471	40.135	40.197	40.271	40.412

Scale	Metrics	Bicubic	GDRRN[17]	3D-FCNN[21]	EDSR[59]	SSPSR[25]	MCNet[23]	SRDNet(Our)
	SSIM \uparrow	0.9638	0.9649	0.9683	0.9784	0.9790	0.9801	0.9807

2) Results on Harvard Dataset

Similar to the results of the CAVE dataset, it can be seen from Table 3 that our SRDNet performs well

in all metrics. In order to clearly display some edge information, the absolute error plot and the spectral fitting plot between Ground truth and the reconstructed hyperspectral image are also used.

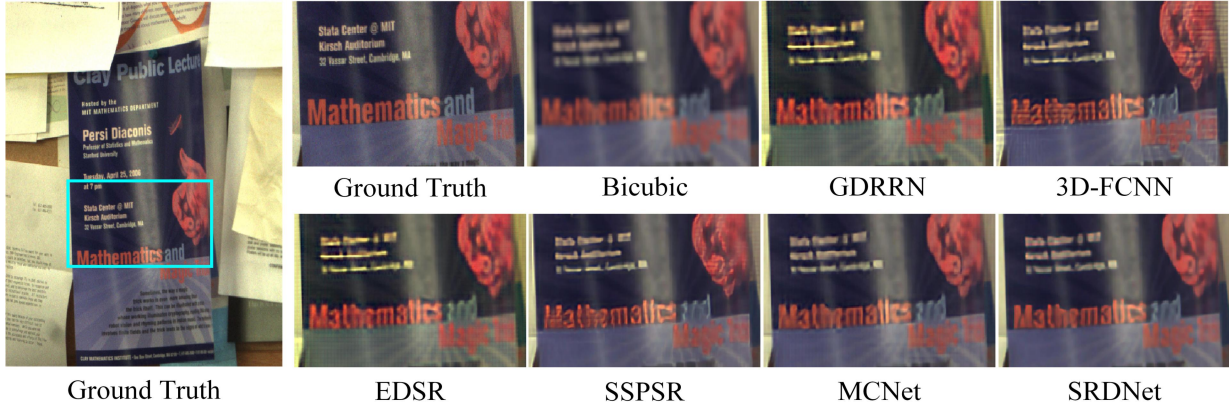


Fig.9. Reconstructed composite images of *img3* in Harvard dataset with spectral bands 23-15-8 as R-G-B when the upsampling factor is 4.

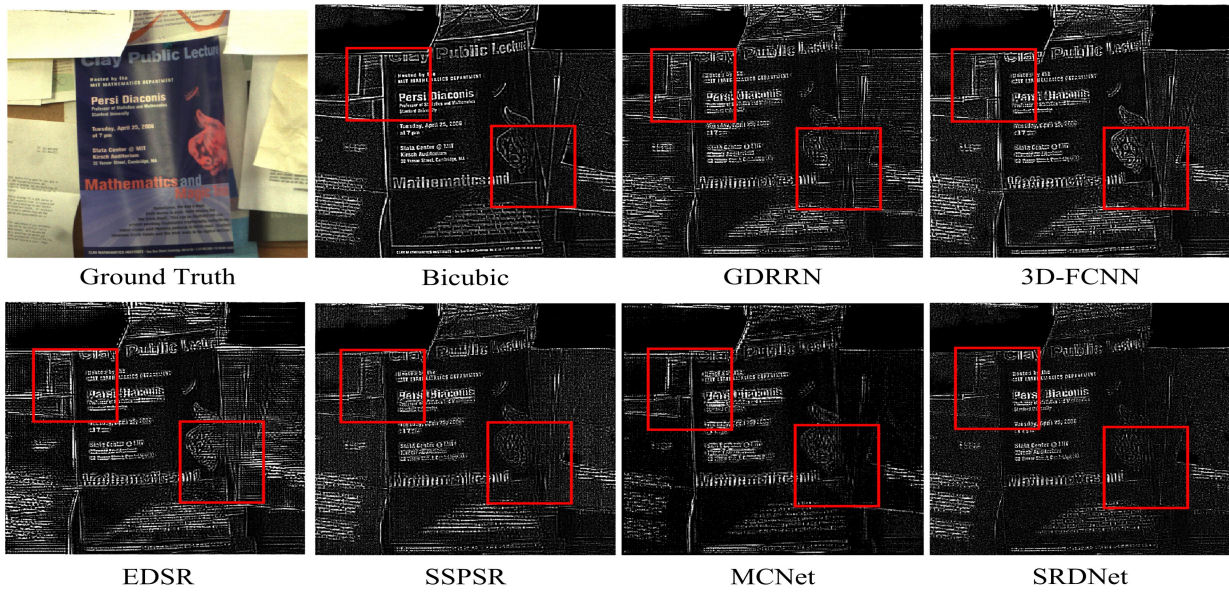
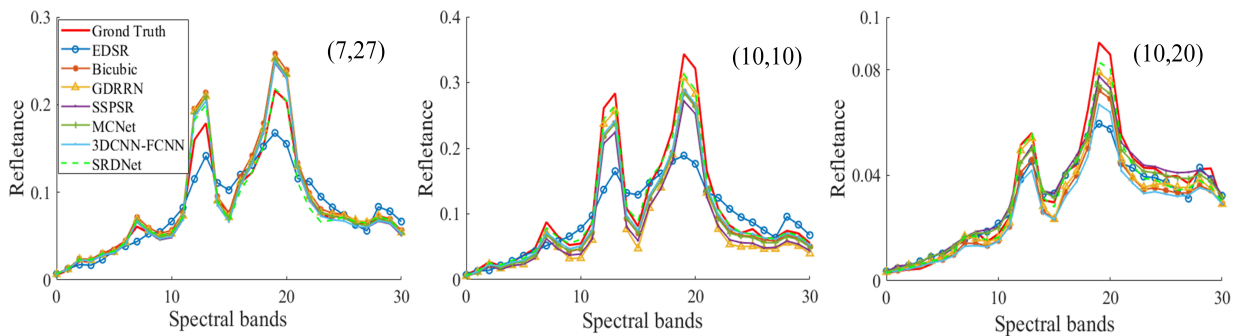


Fig.10. Absolute error map comparisons for *img3* with spectral bands 23-15-8 as R-G-B when the upsampling factor is 4. The less information the image contains, the closer the reconstructed image is to the target image.



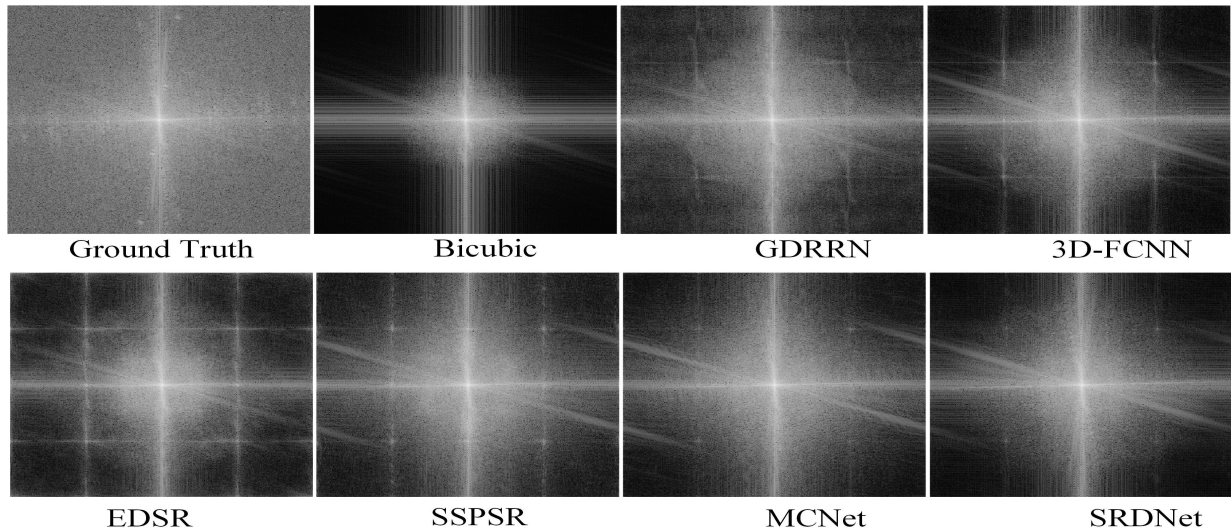


Fig.11 The first row demonstrates a visual comparison of the *img3* image spectral distortion at pixel locations (7, 27), (10, 10) and (10, 20) on the Harvard dataset. The last two rows are the spectral analysis of the *img3* image when the upsampling factor is 4.

For the spectrogram in Fig.11, where the gray background represents high-frequency and the center region represents low-frequency information. In the spectrogram, the high-frequency information of the Bicubic is less than others, so the reconstructed image is blurred, while the high-frequency of MCNet

and SRDNet is cleaner than other algorithms. In addition, as can be seen in Fig. 9 and 10 that each algorithm has certain advantages over bicubic, and the algorithm combining 2D and 3D is better than the algorithm that only contains 2D module or 3D module.

TABLE III

QUANTITATIVE EVALUATION OF 25 TEST IMAGES FOR 6 PQIS ON HARVARD DATA. RED AND BLUE SHOW THE BEST AND SECOND BEST PERFORMANCE RESPECTIVELY.

Scale	Metrics	Bicubic	GDRRN[17]	3D-FCNN[21]	EDSR[59]	SSPSR[25]	MCNet[23]	SRDNet(Our)
×2	CC↑	0.983	0.998	0.998	0.997	0.997	0.998	0.998
	SAM↓	3.091	2.284	2.313	2.867	2.718	2.236	2.218
	RMSE↓	0.006	0.004	0.004	0.005	0.005	0.003	0.003
	ERGAS↓	2.732	1.761	1.727	2.089	2.022	1.522	1.461
	PSNR↑	42.557	45.300	45.620	44.557	44.876	46.845	47.105
	SSIM↑	0.9728	0.9889	0.9874	0.9808	0.9813	0.9893	0.9905
×3	CC↑	0.979	0.995	0.994	0.994	0.996	0.997	0.997
	SAM↓	4.262	3.214	3.073	3.914	2.958	2.549	2.443
	RMSE↓	0.011	0.009	0.009	0.009	0.006	0.005	0.004
	ERGAS↓	4.057	3.433	3.154	3.149	2.555	2.287	2.048
	PSNR↑	38.714	41.070	40.839	40.864	42.900	43.742	43.951
	SSIM↑	0.9485	0.9712	0.9690	0.9691	0.9753	0.9837	0.9846
×4	CC↑	0.976	0.994	0.994	0.991	0.994	0.996	0.996
	SAM↓	4.477	3.206	3.169	4.236	2.814	2.770	2.756
	RMSE↓	0.012	0.008	0.008	0.010	0.008	0.007	0.006
	ERGAS↓	4.069	3.467	3.220	3.761	3.172	2.657	2.644
	PSNR↑	37.815	38.631	38.692	38.407	39.806	42.841	42.902
	SSIM↑	0.9397	0.9669	0.9675	0.9651	0.9749	0.9804	0.9813

As for the Harvard dataset, the table 3 demonstrates the average performances of the various algorithms. It can be observed that the SRDNet outperforms other methods on all the 3 upsampling factors. Among these algorithms, MCNet uses a combination of 2D convolution and 3D convolution to perform the SR task, and we find that it outperforms networks that use only 2D convolution or only 3D convolution. This is that 3D convolution

effectively utilize the frequency spectrum to improve feature exploration, while 2D convolution can effectively improve spatial resolution. Specifically, an upsampling factor of 2/3/4, the PSNR and SSIM of the SRDNet algorithm are 0.260dB/0.0012, 0.209dB/0.0009 and 0.061dB/ 0.0009 higher than the second method (MCNet), respectively.

3) Results on Chikusei Dataset

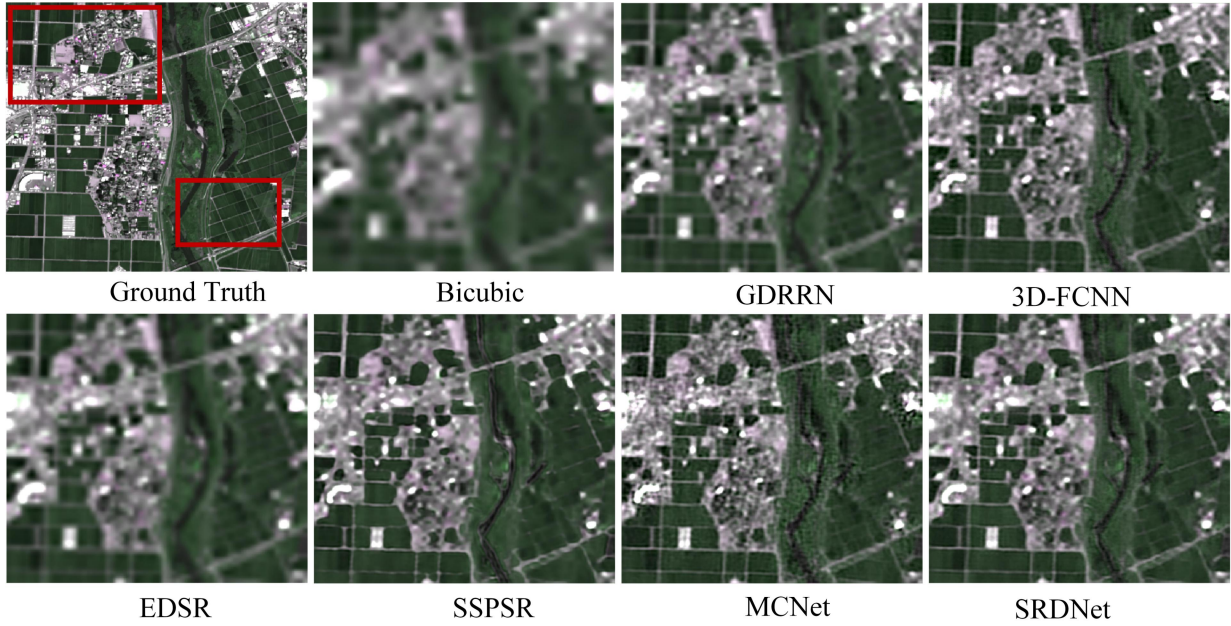


Fig.12. Reconstructed the *Chikusei_test_1* image of in Chikusei dataset with spectral bands 55-45-55 as R-G-B when the upsampling factor is 8.

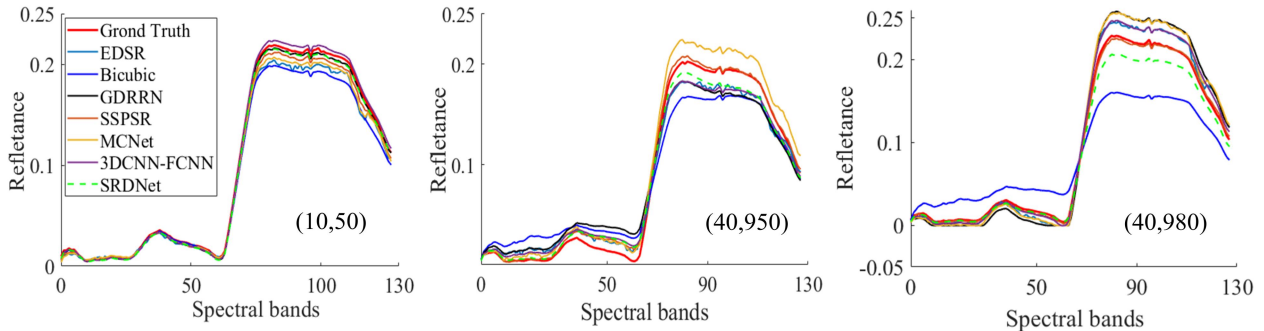


Fig.13. The visual comparison of the *Chikusei_test_1* image image spectral distortion at pixel locations (10, 50), (27, 127) and (40, 950) on the Chikusei dataset.

Unlike the previous two datasets, the Chikusei dataset is 128 channels. To test the effect of each algorithm when the upsampling factor is large, the 4 and the 8 are selected for the upsampling factor. Figures 12 and 13 show the reconstructed images and spectral fit images of the seven most competitive algorithms on the Chikusei dataset, separately. The results of EDSR [59], GDRRN [17], and Bicubic are very vague, and the SRDNet algorithm can recon-

struct the main structural features and spectral information of the image. It should be noted that spectral distortion and texture blurring are worse when the upsampling factor is large. In other words, an upsampling factor of 8 gives worse visual results compared to an upsampling factor of 4.

The table 4 illustrates the average performances of all comparison algorithms on the four test images. It can be seen that the SRDNet is significantly superior

to other algorithms except SSPSR[25]. However, the SSPSR algorithm, as described in the previous two datasets, does not perform very well during the number of images is large. Moreover, the large number of network parameters of the SSPSR makes the computation expensive and affects the convergence time of the model. The small number of images in the Chikusei dataset affects the performance of the SRDNet and the MCNet algorithms. This is one of

the main drawbacks of these CNN-based approaches. In order to obtain a model with good generalization ability, a great amount of samples are trained. EDSR networks that perform well in RGB image SR can achieve satisfactory results, but compared with these single hyperspectral algorithms, namely 3D-FCNN [21] and GDRRN [17] and MCNet [23], its SAM index is relatively poor.

TABLE IV

DIFFERENT APPROACHES FOR THE 4 PQIS PAIRS OF TEST IMAGES ON THE CHIKUSEI DATASET. RED AND BLUE SHOW THE BEST AND SECOND BEST PERFORMANCE RESPECTIVELY.

Scale	Metrics	Bicubic	GDRRN[17]	3D-FCNN[21]	EDSR[59]	SSPSR[25]	MCNet[23]	SRDNet(Our)
×4	CC↑	0.883	0.975	0.978	0.977	0.982	0.979	0.981
	SAM↓	4.317	3.324	3.201	3.462	2.672	3.009	2.659
	PSNR↑	33.869	36.767	37.363	37.252	38.210	37.657	37.982
	SSIM↑	0.8135	0.9049	0.9179	0.9173	0.9312	0.9196	0.9286
×8	CC↑	0.832	0.945	0.945	0.938	0.952	0.947	0.950
	SAM↓	6.427	4.922	4.894	5.534	4.404	4.842	4.435
	PSNR↑	31.174	33.381	33.502	32.960	33.960	33.606	33.854
	SSIM↑	0.7438	0.8274	0.8313	0.8193	0.8474	0.8366	0.8468

C. Ablation Study

TABLE V

ABLATION STUDIES ON COMPONENTS, WHERE 'W/O' INDICATES THAT THIS MODULE IS NOT INCLUDED.

Method	Module	Component	CC↑	SAM↓	PSNR↑	SSIM↑
Our	Our-3D-uint(×)	Baseline	0.983	2.884	42.469	0.9847
	Our-2D-uint(×)					
Our	Our-3D-uint(√)	Two 3D-uint	0.987	2.741	42.925	0.9863
		Three 3D-uint	0.988	2.672	42.944	0.9869
	Our-2D-uint(√)	Four 3D-uint	0.987	2.679	42.937	0.9867
		Three 3D-uint	0.985	2.793	42.611	0.9848
Our-w/o	Our-3D-uint(√)	IGM(√) HSL(×)	0.986	2.776	42.739	0.9859
	Our-2D-uint(×)					
PAM module	Our-3D-uint(×)	IGM(×) HSL(√)	0.984	2.883	42.574	0.9850
	Our-2D-uint(√)	IGM(√) HSL(√)	0.986	2.765	42.742	0.9861
Our-Loss	Our-w/o HFL	L1	0.988	2.681	42.913	0.9869
		L1+L _{HFL}	0.988	2.672	42.944	0.9869

As described in subsection III, our method consists of four main components, where the PAM block is the main part of the entire network for

feature extraction. We call the rest of the network after removing the PAM module the baseline.

In this subsection, the effect of different combinations of PAM on model performance is investigated. Table 5 displays the ablation studies for these combinations at the upsampling factor of 3 in the CAVE dataset (*fake_and_real_lemons_ms*). Specifically, when the PAM module is removed from the network, the network performs less well for the same number of parameters. When the PAM module has only 3D units, the results are not very satisfactory.

This is the result of the network focusing too much on spectral information at the expense of spatial resolution. When the PAM contains both 2D convolution and 3D convolution units, the effectiveness is significantly better than the 2D unit alone. The above illustrates that the combination of 2D and 3D units can improve the spatial expression of the network.

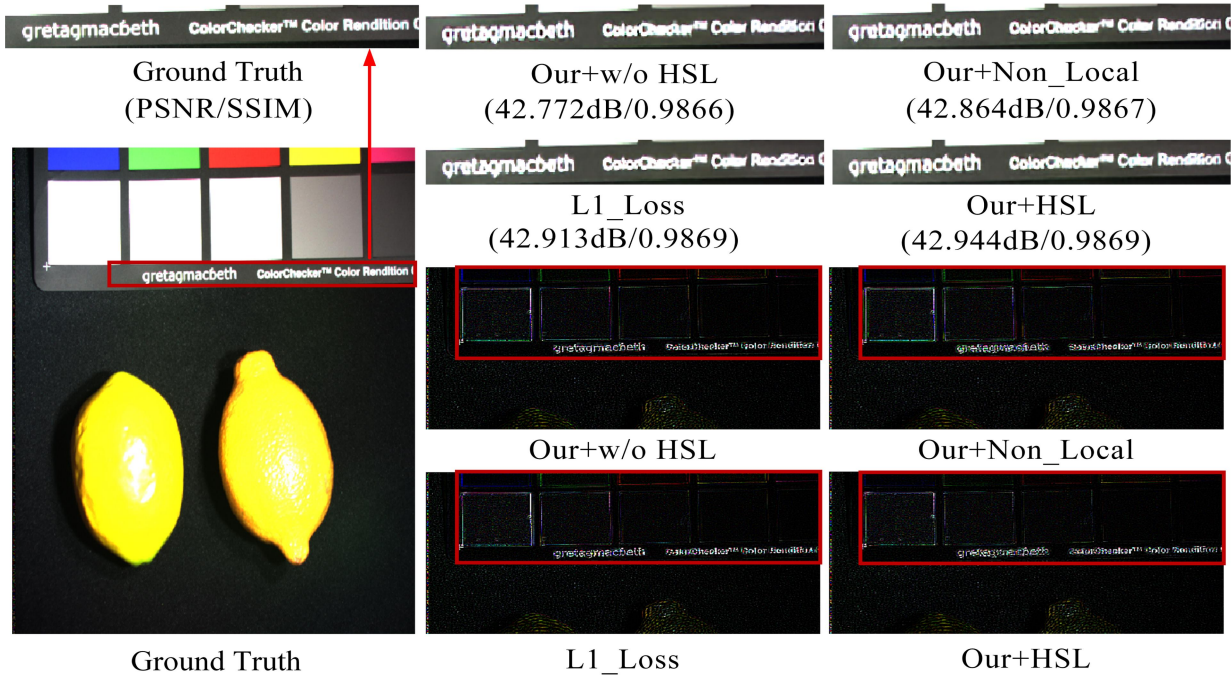


Fig.14 The first two rows are the reconstructed image of the *fake_and_real_lemons_ms* in the CAVE set when an upsampling factor of $d=3$, with spectral bands 23-15-8 as R-G-B. The last two lines are the absolute error map comparison of the *fake_and_real_lemons_ms*. The less information the picture contains, the closer the reconstructed image is to the target image. Where 'w/o' indicates that this module is not included.

As can be seen in Fig. 14, in the frequency domain, the inclusion of the HFL makes the network to focus on difficult frequencies and thus reconstruct quality. That is, the absolute error of including HEL loss has less than that of including only L_1 loss. On the other hand, it can be observed that the HSL module in this article can improve the reconstruction quality of the image. And even compared with the classical non-local attention mechanism (Non_Local), our proposed HSL has some advantages, and the absolute error information is less than the former. At the end, all components are combined to the model, and it can be seen that all three aspects outperform any other combination. Thus with these analyses, each component contributes to model learning and optimization.

V. CONCLUSION

In this article, a hyperspectral image super-resolution algorithm by dual-domain network (SRDNet) is proposed. To acquire more spatial information when learning spectral information, our method employs a hybrid convolution of 2D and 3D units with progressive upsampling during reconstruction. Different from previous work, a dual-domain learning network is designed. The spectral self-attention mechanism is adopted to adaptively select important spectral information, and is able to the network that obtains fine and continuous pixel-level features. Besides, to resolve the visual discrepancy generated by pixel-level loss, a frequency loss is adopted to narrow the frequency domain

difference between the reconstructed image and the ground truth. The dynamic weighting mechanism enables the network to focus on fine-grained frequencies, promoting the perceptual quality of HSI. The effectiveness of various modules in enhancing spatial information and spectral coherence are verified in ablation studies.

Visual analysis and quantitative experiments of three common hyperspectral datasets demonstrate that the SRDNet achieves excellent performance in HSI reconstruction at the pixel level as well as at the frequency level. Our algorithm achieves optimal performance in a number of commonly objective metrics, and the images are perceptually less different from ground truth than other methods.

REFERENCES

- [1] H. Peng, X. Chen, and J. Zhao, "Residual Pixel Attention Network for Spectral Reconstruction from RGB Images," presented at the 2020 IEEE/CVF Conference on Computer Vision and Pattern Recognition Workshops (CVPRW), 2020.
- [2] T. Wang, Z. Zhu, and E. Blasch, "Bio-Inspired Adaptive Hyperspectral Imaging for Real-Time Target Tracking," *IEEE Sensors Journal*, vol. 10, no. 3, pp. 647-654, 2010, doi: 10.1109/jсен.2009.2038657.
- [3] Z. Khan, F. Shafait, and A. Mian, "Automatic ink mismatch detection for forensic document analysis," *Pattern Recognition*, vol. 48, no. 11, pp. 3615-3626, 2015, doi: 10.1016/j.patcog.2015.04.008.
- [4] M. T. Eismann, J. Meola, and R. C. Hardie, "Hyperspectral Change Detection in the Presence of Diurnal and Seasonal Variations," *IEEE Transactions on Geoscience and Remote Sensing*, vol. 46, no. 1, pp. 237-249, 2008, doi: 10.1109/tgrs.2007.907973.
- [5] X. Xu, J. Li, X. Huang, M. Dalla Mura, and A. Plaza, "Multiple Morphological Component Analysis Based Decomposition for Remote Sensing Image Classification," *IEEE Transactions on Geoscience and Remote Sensing*, vol. 54, no. 5, pp. 3083-3102, 2016, doi: 10.1109/tgrs.2015.2511197.
- [6] Y. Chen, N. M. Nasrabadi, and T. D. Tran, "Hyperspectral Image Classification Using Dictionary-Based Sparse Representation," *IEEE Transactions on Geoscience and Remote Sensing*, vol. 49, no. 10, pp. 3973-3985, 2011, doi: 10.1109/tgrs.2011.2129595.
- [7] J. F. Hu, T. Z. Huang, L. J. Deng, T. X. Jiang, G. Vivone, and J. Chanussot, "Hyperspectral Image Super-Resolution via Deep Spatiospectral Attention Convolutional Neural Networks," *IEEE Trans Neural Netw Learn Syst*, vol. 33, no. 12, pp. 7251-7265, Dec 2022, doi: 10.1109/TNNLS.2021.3084682.
- [8] N. Yokoya, C. Grohnfeldt, and J. Chanussot, "Hyperspectral and Multispectral Data Fusion A comparative review of the recent literature," (in English), *Ieee Geoscience and Remote Sensing Magazine*, vol. 5, no. 2, pp. 29-56, Jun 2017, doi: 10.1109/Mgrs.2016.2637824.
- [9] P. Ghamisi *et al.*, "Advances in Hyperspectral Image and Signal Processing: A Comprehensive Overview of the State of the Art," *IEEE Geoscience and Remote Sensing Magazine*, vol. 5, no. 4, pp. 37-78, 2017, doi: 10.1109/mgrs.2017.2762087.
- [10] O. Gomez, O. Ibanez, A. Valsecchi, and O. Cordon, "Improving Comparative Radiography by Multi-resolution 3D-2D Evolutionary Image Registration," (in English), *Lect Notes Artif Int*, vol. 11734, pp. 99-110, 2019, doi: 10.1007/978-3-030-29859-3_9.
- [11] J. Li *et al.*, "Hyperspectral Image Super-Resolution by Band Attention Through Adversarial Learning," *IEEE Transactions on Geoscience and Remote Sensing*, vol. 58, no. 6, pp. 4304-4318, 2020, doi: 10.1109/tgrs.2019.2962713.
- [12] L. Bungert, D. A. Coomes, M. J. Ehrhardt, J. Rasch, R. Reisenhofer, and C.-B. Schönlieb, "Blind image fusion for hyperspectral imaging with the directional total variation," *Inverse Problems*, vol. 34, no. 4, 2018, doi: 10.1088/1361-6420/aaaf63.
- [13] K. Zhang, M. Wang, S. Yang, and L. Jiao, "Spatial-Spectral-Graph-Regularized Low-Rank Tensor Decomposition for Multi-spectral and Hyperspectral Image Fusion," *IEEE Journal of Selected Topics in Applied Earth Observations and Remote Sensing*, vol. 11, no. 4, pp. 1030-1040, 2018, doi: 10.1109/jstars.2017.2785411.
- [14] S. Li, R. Dian, L. Fang, and J. M. Bioucas-Dias, "Fusing Hyperspectral and Multispectral Images via Coupled Sparse Tensor Factorization," *IEEE Trans Image Process*, May 15 2018, doi: 10.1109/TIP.2018.2836307.
- [15] X. Dou, C. Li, Q. Shi, and M. Liu, "Super-Resolution for Hyperspectral Remote Sensing Images Based on the 3D Attention-SRGAN Network," *Remote Sensing*, vol. 12, no. 7, 2020, doi: 10.3390/rs12071204.
- [16] P. V. Arun, K. M. Buddhiraju, A. Porwal, and J. Chanussot, "CNN-Based Super-Resolution of Hyperspectral Images," *IEEE Transactions on Geoscience and Remote Sensing*, vol. 58, no. 9, pp. 6106-6121, 2020, doi: 10.1109/tgrs.2020.2973370.
- [17] Y. Li, L. Zhang, C. Ding, W. Wei, and Y. N. Zhang, "Single Hyperspectral Image Super-resolution with Grouped Deep Recursive Residual Network," (in English), *2018 Ieee Fourth International Conference on Multimedia Big Data (Bigmm)*, 2018.[Online]. Available: <Go to ISI>://WOS: 0006304 23400041.

- [18] Y. Tai, J. Yang, and X. M. Liu, "Image Super-Resolution via Deep Recursive Residual Network," (in English), *Proc Cvrpr Ieee*, pp. 2790-2798, 2017, doi: 10.1109/Cvpr.2017.298.
- [19] J. Jia, L. Ji, Y. Zhao, and X. Geng, "Hyperspectral image super-resolution with spectral-spatial network," *International Journal of Remote Sensing*, vol. 39, no. 22, pp. 7806-7829, 2018, doi: 10.1080/01431161.2018.1471546.
- [20] J. Li, R. Cui, B. Li, R. Song, Y. Li, and Q. Du, "Hyperspectral Image Super-Resolution with 1D-2D Attentional Convolutional Neural Network," *Remote Sensing*, vol. 11, no. 23, 2019, doi: 10.3390/rs11232859.
- [21] S. Mei, X. Yuan, J. Ji, Y. Zhang, S. Wan, and Q. Du, "Hyperspectral Image Spatial Super-Resolution via 3D Full Convolutional Neural Network," *Remote Sensing*, vol. 9, no. 11, 2017, doi: 10.3390/rs9111139.
- [22] Yang, Zhao, Chan, and Xiao, "A Multi-Scale Wavelet 3D-CNN for Hyperspectral Image Super-Resolution," *Remote Sensing*, vol. 11, no. 13, 2019, doi: 10.3390/rs11131557.
- [23] Q. Li, Q. Wang, and X. Li, "Mixed 2D/3D Convolutional Network for Hyperspectral Image Super-Resolution," *Remote Sensing*, vol. 12, no. 10, 2020, doi: 10.3390/rs12101660.
- [24] Z. Zhong, J. Li, Z. Luo, and M. Chapman, "Spectral-Spatial Residual Network for Hyperspectral Image Classification: A 3-D Deep Learning Framework," *IEEE Transactions on Geoscience and Remote Sensing*, vol. 56, no. 2, pp. 847-858, 2018, doi: 10.1109/tgrs.2017.2755542.
- [25] R. T. Jiang *et al.*, "Learning Spectral and Spatial Features Based on Generative Adversarial Network for Hyperspectral Image Super-Resolution," (in English), *Int Geosci Remote Se*, pp. 3161-3164, 2019. [Online]. Available: <Go to ISI>://WOS: 000519270603048.
- [26] Q. Wang, Q. Li, and X. Li, "Hyperspectral Image Superresolution Using Spectrum and Feature Context," *IEEE Transactions on Industrial Electronics*, vol. 68, no. 11, pp. 11276-11285, 2021, doi: 10.1109/tie.2020.3038096.
- [27] Q. Li, Q. Wang, and X. L. Li, "Exploring the Relationship Between 2D/3D Convolution for Hyperspectral Image Super-Resolution," (in English), *Ieee Transactions on Geoscience and Remote Sensing*, vol. 59, no. 10, pp. 8693- 8703, Oct 2021, doi: 10.1109/Tgrs.2020.3047363.
- [28] Y. Wang, X. A. Chen, Z. Han, and S. Y. He, "Hyperspectral Image Super-Resolution via Nonlocal Low-Rank Tensor Approximation and Total Variation Regularization," (in English), *Remote Sensing*, vol. 9, no. 12, Dec 2017, doi: ARTN 128610.3390/rs9121286.
- [29] Y. Wang, J. Peng, Q. Zhao, Y. Leung, X.-L. Zhao, and D. Meng, "Hyperspectral Image Restoration Via Total Variation Regularized Low-Rank Tensor Decomposition," *IEEE Journal of Selected Topics in Applied Earth Observations and Remote Sensing*, vol. 11, no. 4, pp. 1227-1243, 2018, doi: 10.1109/jstars.2017.2779539.
- [30] H. J. Huang, J. Yu, and W. D. Sun, "Super-Resolution Mapping Via Multi-Dictionary Based Sparse Representation," (in English), *Int Conf Acoust Spee*, 2014. [Online]. Available: <Go to ISI>://WOS:000343655303114.
- [31] W. Xie, X. Jia, Y. Li, and J. Lei, "Hyperspectral Image Super-Resolution Using Deep Feature Matrix Factorization," *IEEE Transactions on Geoscience and Remote Sensing*, vol. 57, no. 8, pp. 6055-6067, 2019, doi: 10.1109/tgrs.2019.2904108.
- [32] Y. Yuan, X. Zheng, and X. Lu, "Hyperspectral Image Super-resolution by Transfer Learning," *IEEE Journal of Selected Topics in Applied Earth Observations and Remote Sensing*, vol. 10, no. 5, pp. 1963-1974, 2017, doi: 10.1109/jstars.2017.2655112.
- [33] J. Hu, X. Jia, Y. Li, G. He, and M. Zhao, "Hyperspectral Image Super-Resolution via Intrafusion Network," *IEEE Transactions on Geoscience and Remote Sensing*, vol. 58, no. 10, pp. 7459-7471, 2020, doi: 10.1109/tgrs.2020.2982940.
- [34] K. Zheng *et al.*, "Separable-spectral convolution and inception network for hyperspectral image super-resolution," *International Journal of Machine Learning and Cybernetics*, vol. 10, no. 10, pp. 2593-2607, 2019, doi: 10.1007/s13042-018-00911-4.
- [35] J. Hu, L. Shen, and G. Sun, "Squeeze-and-Excitation Networks," presented at the 2018 IEEE/CVF Conference on Computer Vision and Pattern Recognition, 2018.
- [36] S. H. Woo, J. Park, J. Y. Lee, and I. S. Kweon, "CBAM: Convolutional Block Attention Module," (in English), *Lect Notes Comput Sc*, vol. 11211, pp. 3-19, 2018, doi:10.1007/978-3-030-01234-2_1.
- [37] M. U. Yaseen, M. M. Nasralla, F. Aslam, S. S. Ali, and S. B. Khattak, "A Novel Approach Based on Multi-Level Bottleneck Attention Modules Using Self-Guided Dropblock for Person Re-Identification," (in English), *Ieee Access*, vol. 10, pp. 123160-123176, 2022, doi: 10.1109/Access.2022.3223426.
- [38] D. Liu, J. Li, and Q. Yuan, "A Spectral Grouping and Attention-Driven Residual Dense Network for Hyperspectral Image Super-Resolution," *IEEE Transactions on Geoscience and Remote Sensing*, vol. 59, no. 9, pp. 7711-7725, 2021, doi: 10.1109/tgrs.2021.3049875.
- [39] D. Martin, C. Fowlkes, D. Tal, and J. Malik, "A database of human segmented natural images and its application to evaluating segmentation algorithms and measuring ecological statistics[38]," (in English), *Eighth Ieee International Conference on Computer Vision, Vol Ii, Proceedings*, pp. 416-423, 2001, doi: DOI 10.1109/iccv.2001.937655.
- [40] Y. Hu, J. Li, Y. Huang, and X. Gao, "Channel-Wise and Spatial Feature Modulation Network for Single Image Super-Resolution," *IEEE Transactions on Circuits and Systems for Video Technology*,

- vol. 30, no. 11, pp. 3911-3927, 2020, doi: 10.1109/ tcsvt. 2019. 2915238.
- [41] M.-a. Li, Y.-x. Dong, Y.-j. Sun, J.-f. Yang, and L.-j. Duan, "Subject-based dipole selection for decoding motor imagery tasks," *Neurocomputing*, vol. 402, pp. 195-208, 2020, doi: 10.1016/j.neucom.2020.03.055.
- [42] T. Dai, J. Cai, Y. Zhang, S.-T. Xia, and L. Zhang, "Second- Order Attention Network for Single Image Super- Resolution," presented at the 2019 IEEE/CVF Conference on Computer Vision and Pattern Recognition (CVPR), 2019.
- [43] Y. Chen *et al.*, "Image super-resolution reconstruction based on feature map attention mechanism," *Applied Intelligence*, vol. 51, no. 7, pp. 4367-4380, 2021, doi: 10.1007/s10489-020-02116-1.
- [44] S. E. Chang, Y. Chen, Y. C. Yang, E. T. Lin, P. Y. Hsiao, and L. C. Fu, "SE-PSNet: Silhouette-based Enhancement Feature for Panoptic Segmentation Network," (in English), *J Vis Commun Image R*, vol. 90, Feb 2023, doi: ARTN 10373610. 1016/ j. jvcir. 2022.103736.
- [45] H. J. Liu, F. Q. Liu, X. Y. Fan, and D. Huang, "Polarized self-attention: Towards high-quality pixel-wise mapping," (in English), *Neurocomputing*, vol. 506, pp. 158-167, Sep 28 2022, doi: 10.1016/j.neucom.2022.07.054.
- [46] T. Xie, Y. M. Du, T. Wang, B. H. Hao, Q. Liu, and X. L. Tang, "Structure Improved Conditional Spectral Normalization Generative Adversarial Networks for Image Recognition," (in English), *Chin Autom Congr*, pp. 842-846, 2020, doi: 10.1109/ Cac51589.2020.9327455.
- [47] B. Mildenhall, P. P. Srinivasan, M. Tancik, J. T. Barron, R. Ramamoorthi, and R. Ng, "NeRF: Representing Scenes as Neural Radiance Fields for View Synthesis," (in English), *Commun Acm*, vol. 65, no. 1, pp. 99-106, Jan 2022. [Online]. Available: <Go to ISI>://WOS:000731456200022.
- [48] L. M. Jiang, B. Dai, W. N. Wu, and C. C. Loy, "Focal Frequency Loss for Image Reconstruction and Synthesis," (in English), *2021 Ieee/Cvf International Conference on Computer Vision (Iccv 2021)*, pp. 13899-13909, 2021, doi: 10.1109/Iccv48922.2021.01366.
- [49] X. Hu *et al.*, "HDNet: High-resolution Dual-domain Learning for Spectral Compressive Imaging," presented at the 2022 IEEE/CVF Conference on Computer Vision and Pattern Recognition (CVPR), 2022.
- [50] M. Fritsche, S. Gu, and R. Timofte, "Frequency Separation for Real-World Super-Resolution," presented at the 2019 IEEE/CVF International Conference on Computer Vision Workshop (ICCVW), 2019.
- [51] J. H. Kim, J. H. Choi, M. Cheon, and J. S. Lee, "MAMNet: Multi-path adaptive modulation network for image super-resolution," (in English), *Neurocomputing*, vol. 402, pp. 38- 49, Aug 18 2020, doi: 10.1016/ j.neucom.2020. 03.069.
- [52] C. Tian, Y. Zhang, W. Zuo, C. W. Lin, D. Zhang, and Y. Yuan, "A Heterogeneous Group CNN for Image Super- Resolution," *IEEE Trans Neural Netw Learn Syst*, vol. PP, Oct 13 2022, doi: 10.1109/ TNNLS.2022.3210433.
- [53] F. Yasuma, T. Mitsunaga, D. Iso, and S. K. Nayar, "Generalized assorted pixel camera: postcapture control of resolution, dynamic range, and spectrum," *IEEE Trans Image Process*, vol. 19, no. 9, pp. 2241-53, Sep 2010, doi: 10.1109/TIP.2010.2046811.
- [54] A. Chakrabarti and T. Zickler, "Statistics of Real-World Hyperspectral Images," (in English), *2011 Ieee Conference on Computer Vision and Pattern Recognition (Cvpr)*, pp. 193-200, 2011. [Online]. Available: <Go to ISI>://WOS: 000295615800026.
- [55] Z. Wang, A. C. Bovik, H. R. Sheikh, and E. P. Simoncelli, "Image quality assessment: from error visibility to structural similarity," *IEEE Trans Image Process*, vol. 13, no. 4, pp. 600-12, Apr 2004, doi: 10.1109/tip.2003.819861.
- [56] L. Loncan *et al.*, "Hyperspectral Pansharpening: A Review," in *IEEE Geoscience and Remote Sensing Magazine*, vol. 3, no. 3, pp. 27-46, Sept. 2015, doi: 10.1109/MGRS. 2015. 2440094.
- [57] C. Yang, J. H. Everitt, and J. M. Bradford, "Yield estimation from hyperspectral imagery using spectral angle mapper (SAM)," (in English), *T Asabe*, vol. 51, no. 2, pp. 729-737, Mar-Apr 2008. [Online]. Available: <Go to ISI>:// WOS:000255929300040.
- [58] V. Ferraris, N. Dobigeon, Q. Wei, and M. Chabert, "Detecting Changes Between Optical Images of Different Spatial and Spectral Resolutions: A Fusion-Based Approach," (in English), *Ieee Transactions on Geoscience and Remote Sensing*, vol. 56, no. 3, pp. 1566-1578, Mar 2018, doi: 10.1109/Tgrs.2017.2765348.
- [59] B. Lim, S. Son, H. Kim, S. Nah, and K. M. Lee, "Enhanced Deep Residual Networks for Single Image Super-Resolution," (in English), *Ieee Comput Soc Conf*, pp. 1132-1140, 2017, doi: 10.1109/Cvprw.2017.151.